nature energy

Supplementary information

https://doi.org/10.1038/s41560-024-01567-x

Elimination of grain surface concavities for improved perovskite thin-film interfaces

In the format provided by the authors and unedited

Table of Contents:

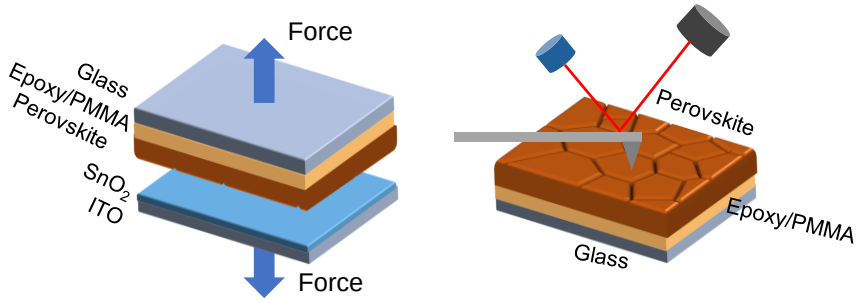

Supplementary Fig. 1. The experimental process for AFM characterizing the delaminated perovskite film bottoms and SnO_2 film tops. Schematic illustration showing the peeling off process and topographic characterization of the bottom surface of perovskite films.

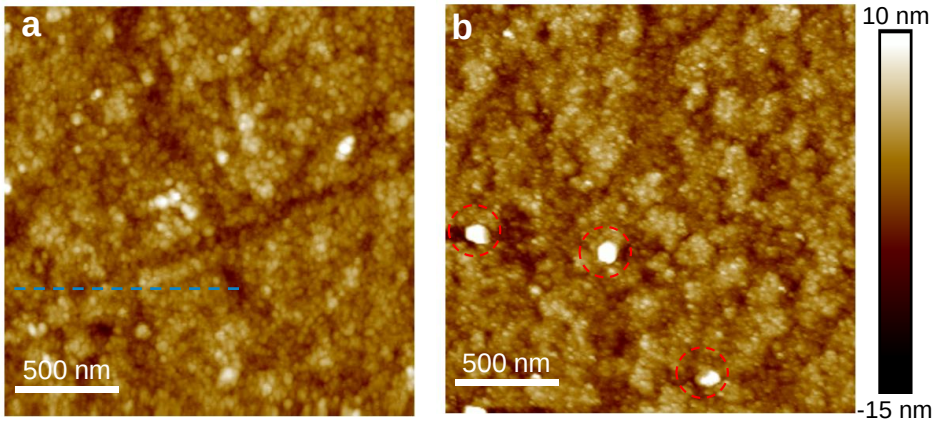

Supplementary Fig. 2. AFM topographies of SnO_2 film surfaces. The 2×2 μm^2 AFM height images of the SnO_2 film surface as-prepared (**a**) and after the peeling off the pristine film from the SnO_2 film (**b**). The red dashed box highlights residual tiny crystal grains on SnO_2 surfaces corresponding to the intragrain holes in **Figure 1a**. The blue dashed line in (**a**) is the guideline of the typical surface height line-profile of the SnO_2 ETL top surface in **Figure g-h**.

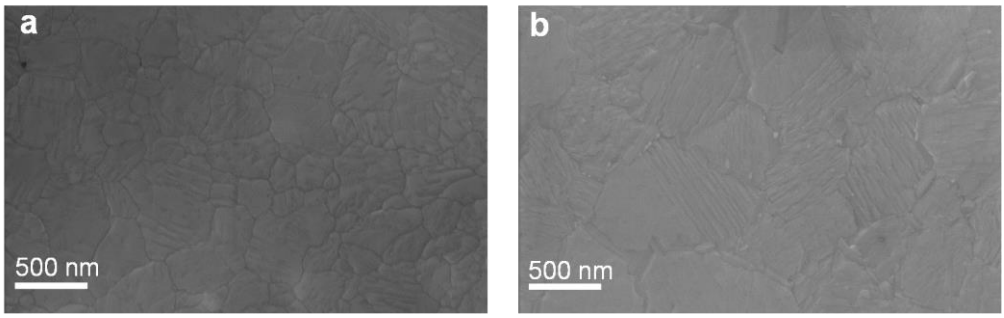

Supplementary Fig. 3. SEM morphologies of perovskite bottom surfaces. The top-view SEM images of the bottom surface of perovskite films with (**a**) and without (**b**) GSCs.

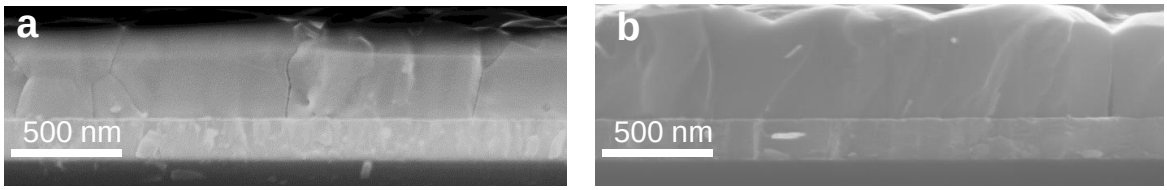

Supplementary Fig. 4. Perovskite heterointerface cross-sections. The cross-sectional SEM images of perovskite grain-CTL heterointerfaces with (**a**) and without (**b**) GSCs.

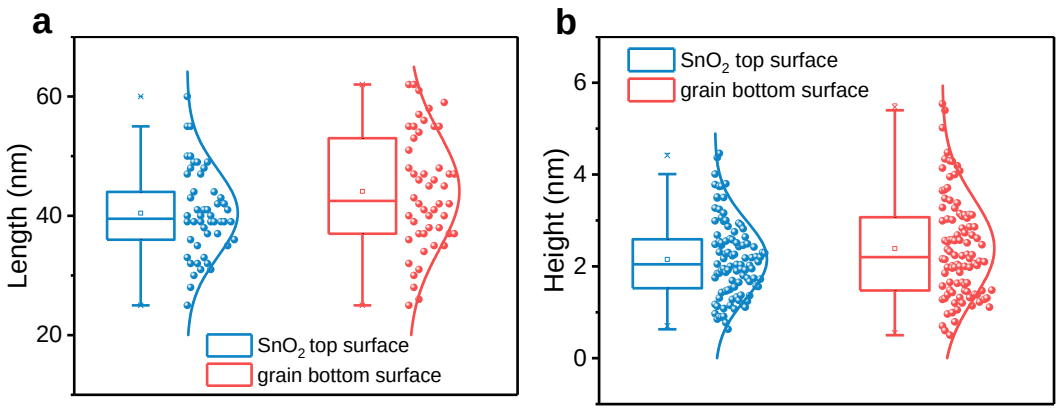

Supplementary Fig. 5. Comparison between SnO_2 top and perovskite grain bottom surface geometry. Statistical distributions of the length (**a**) and height (**b**) localized fluctuations of SnO_2 top micro-surfaces (length, sample size $n = 25$; height, sample size $n = 50$) and grain bottom micro-surfaces (length, sample size $n = 25$; height, sample size $n = 50$) in target group without GSCs. The box plot displays the mean, median line, upper minima and lower maxima, 25~75% box limits with 1.5× interquartile range whiskers.

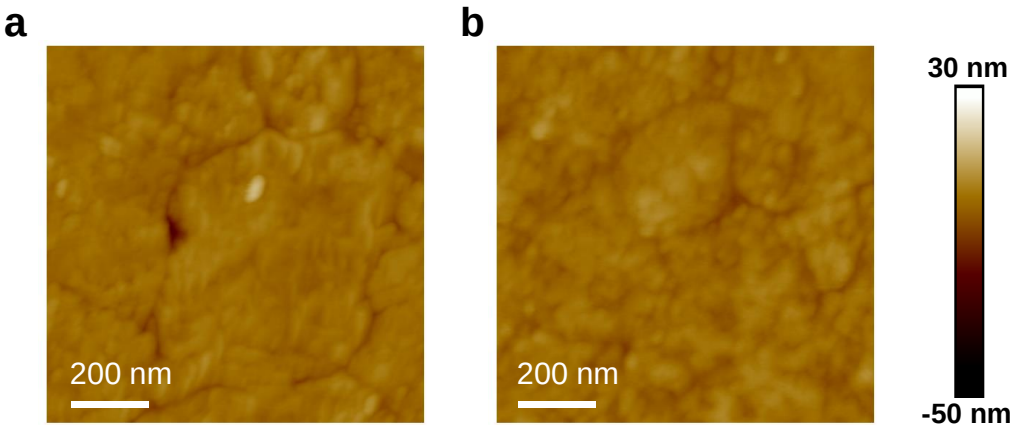

Supplementary Fig. 6. Trivial effect of IPA washing on the AFM topography of perovskite bottom surface. AFM topography (1×1 μm^2) of the perovskite film bottom surfaces of target samples before (**a**) and after (**b**) IPA washing.

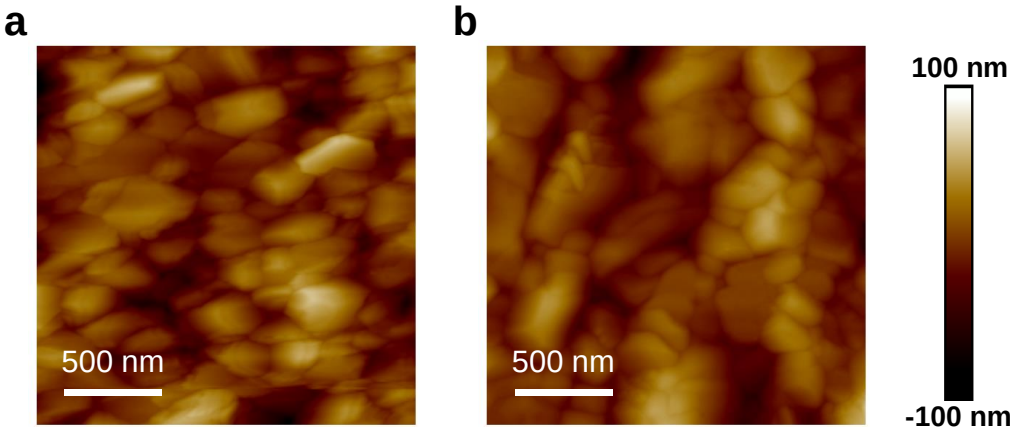

Supplementary Fig. 7. AFM topography of the perovskite top surfaces. The AFM height images of top surface of perovskite films with (**a**) and without GSCs (**b**).

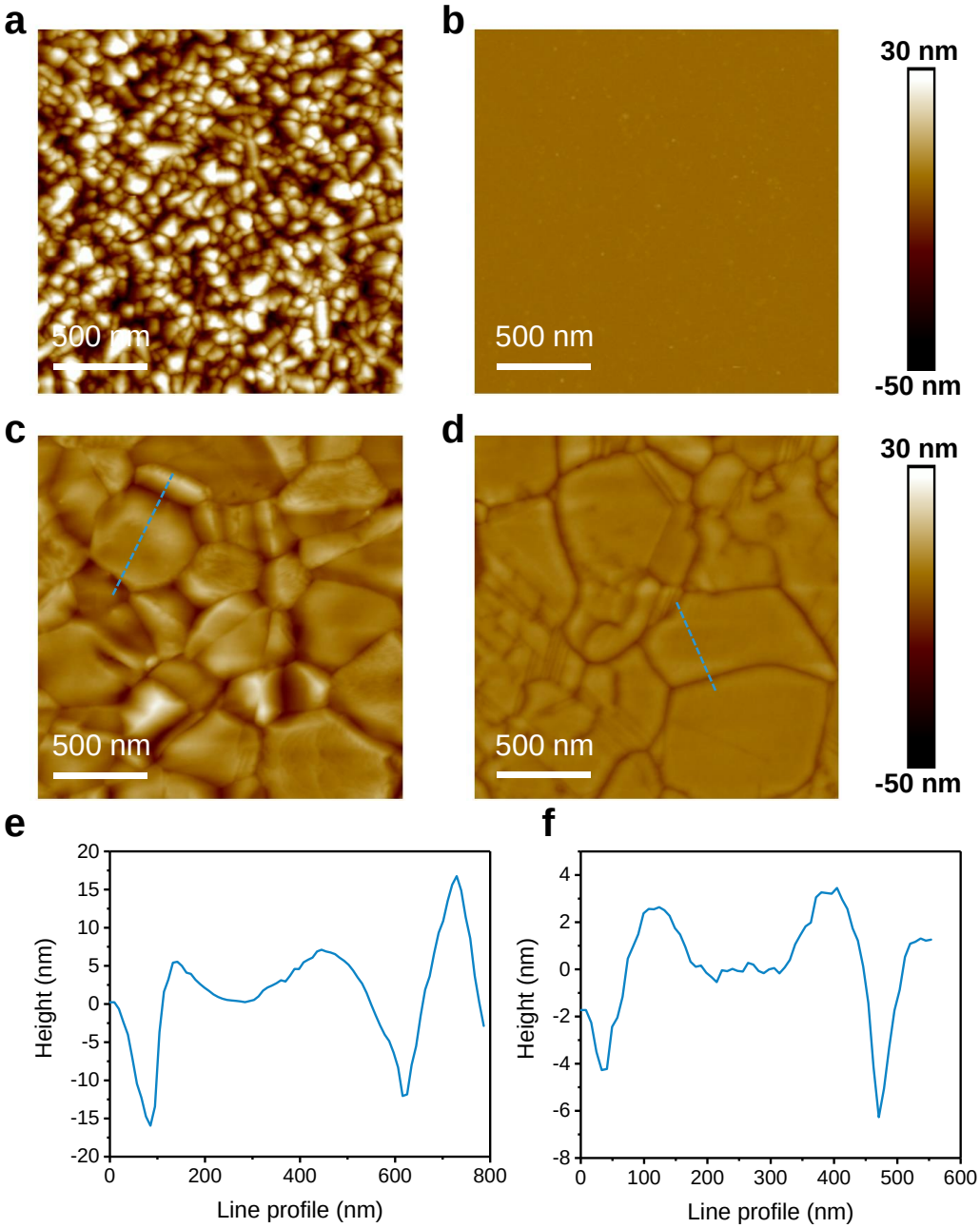

Supplementary Fig. 8. The general GSC existence for perovskite films on different substrates. **a-d,** AFM topography (2×2 μm^2) of the FTO substrate surface (**a**), silicon wafer substrate surface (**b**), and perovskite bottom surface fabricated on FTO (**c**) and silicon wafer (**d**). **e-f,** The 2D height profile guided by blue dashed lines in **Figure c (e)** and **Figure d (f)**.

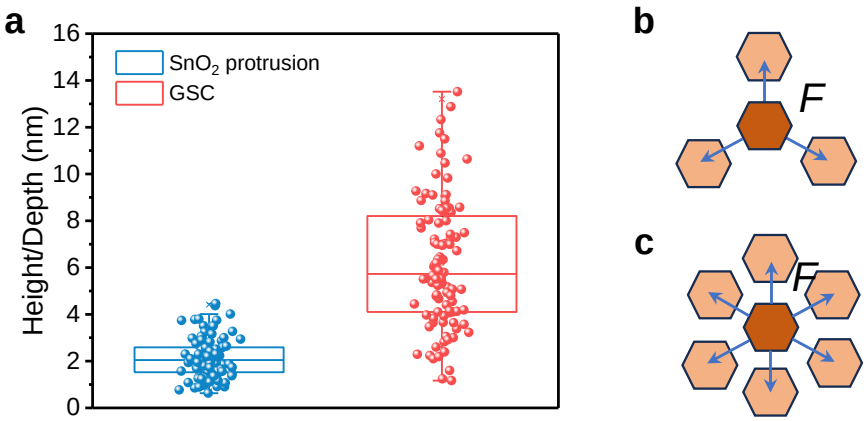

Supplementary Fig. 9. Comparison of SnO_2 protrusion and GSC geometry and schematic illustration of the grain-to-grain variations in GSC geometry. a, The statistical distributions of SnO_2 protrusion height and GSC depth based on total 100 measurements. The box plot displays the mean, median line, upper minima and lower maxima, 25~75% box limits with 1.5× interquartile range whiskers. **b-c**, Schematic illustration of the formation of grains with GSCs of different depths. This discrepancy raise from the different growth conditions for each grain. Some grains grow with influence of interatomic forces from less neighboring grains, resulting in the less of depths of GSCs (**b**), while some grains are influenced by the interatomic forces from more neighboring grains, resulting in a deeper GSC (**c**).

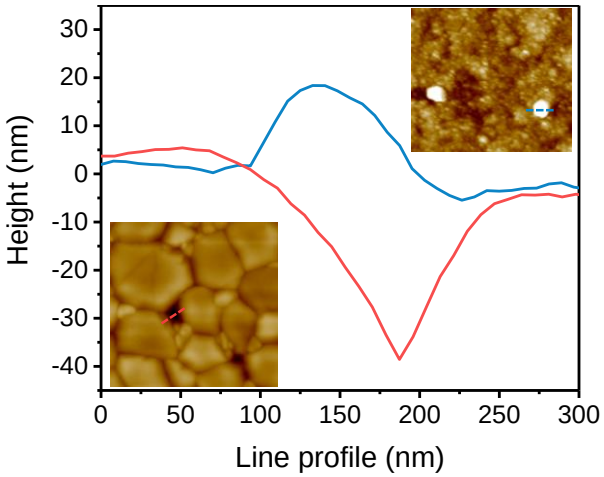

Supplementary Fig. 10. Evidence of residual perovskite nanofragments on SnO_2 surface corresponding to GBGS on perovskite bottom surfaces. The 2D height profile of residual perovskite nanophase on SnO_2 top surface (guided by blue dashed line) and the concave in GBG region on perovskite bottom surface (guided by red dashed line). The left lower AFM height image of perovskite bottom surface was intercepted from **Figure 1a**. The upper right AFM height image of SnO_2 surface was intercepted from **Supplementary Fig. 2b**.

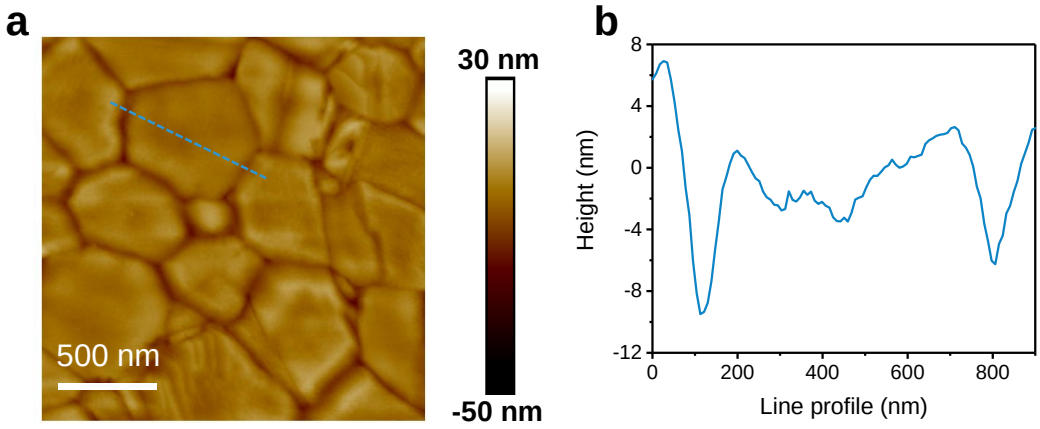

Supplementary Fig. 11. The GSC existence in perovskite films made with KI additives. a, AFM topography of the perovskite film bottom surfaces of samples with additive KI (the same concentration as TFSAP). **b**, The 2D surface height profile guided by blue dashed lines in **a**.

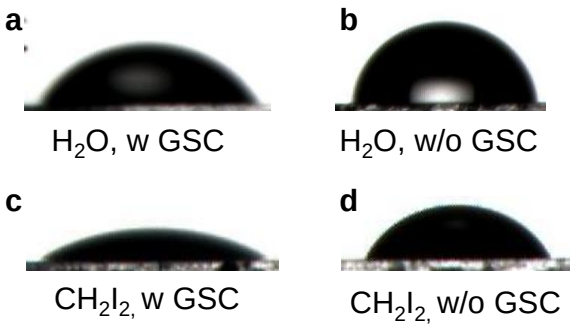

Supplementary Fig. 12. Contact-angle measurement results for estimating surface free energies. Contact angles of H_2O on perovskite films with GSC (**a**) and without GSCs (**b**); and of diiodomethane (CH_2I_2) on perovskite films with GSC (**c**) and without GSCs (**d**).

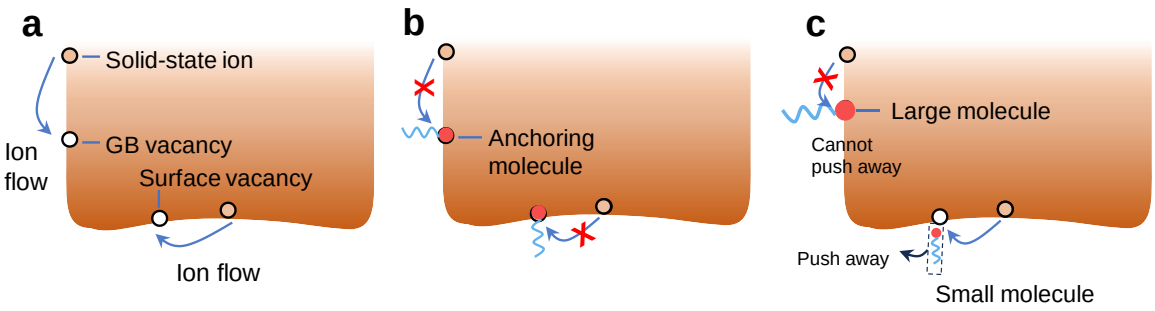

Supplementary Fig. 13. Proposed mechanism for surface-anchored surfactant molecules to retard solid-state ion flow. Schematic illustration of solid-state ion flow on GB and grain surface via vacancy (**a**), the role of anchoring surfactant molecules on suppressing the ion flow (**b**). and the effect of the size of passivation molecule on inhibition of ion flow (**c**). The solid-state ion diffusion is mainly mediated by surface/interface vacancies. The functional groups of surfactant molecules with rich electron pairs can passivate defects in perovskite to hinder ion flow. The moving ions must kinetically push the molecules away to enable the diffusion. A larger passivation molecule will be more difficult to be replaced, leading to a more effective inhibition of solid-state ion migration.

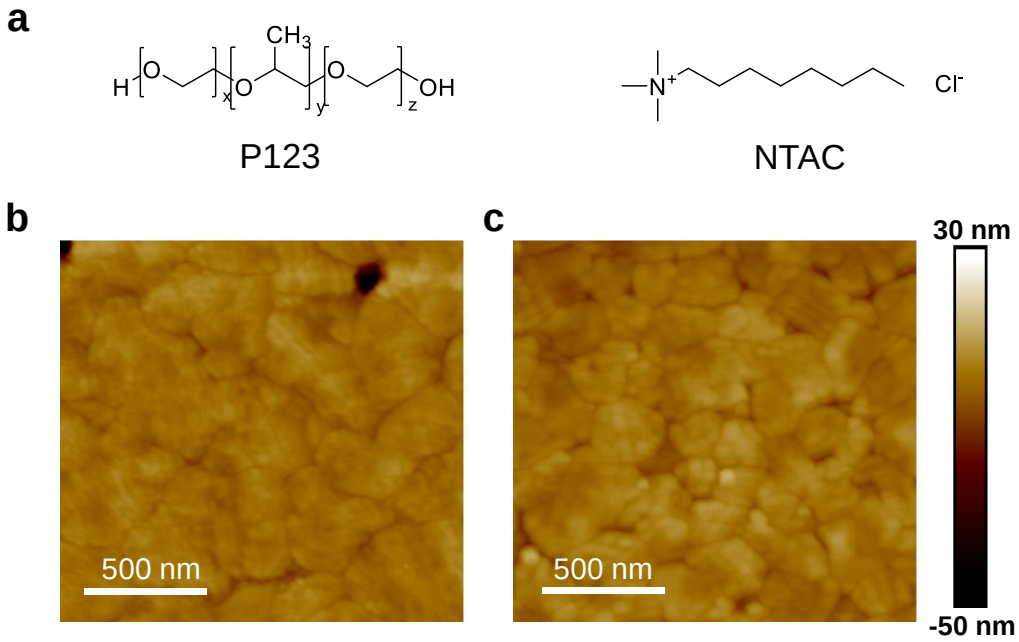

Supplementary Fig. 14. GSCs minimization on perovskite bottom surfaces enabled by other surfactant additives. a, The molecular structures of P123 and NTAC. **b-c**, The AFM topography of the bottom surfaces of perovskite films at the perovskite-CTL heterointerface with additives of P123 (**b**) and NTAC (**c**) into precursor solution.

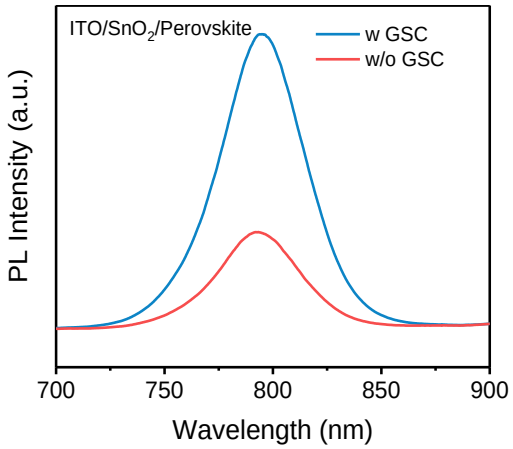

Supplementary Fig. 15. Steady PL measurement results of the glass/SnO_2/perovskite structure. The steady PL intensity of perovskite films with and without GSCs with the structure of glass/SnO_2/perovskite.

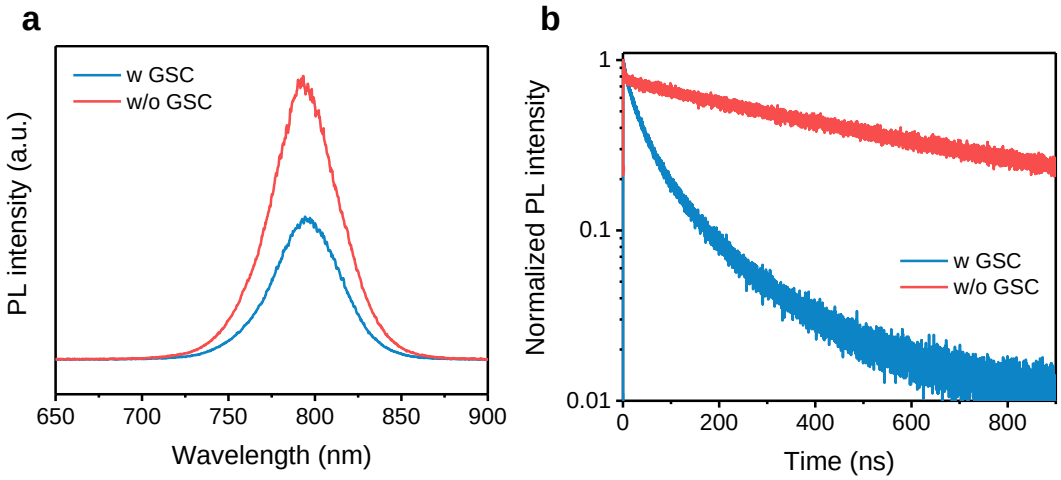

Supplementary Fig. 16. PL and TRPL measurement results of delaminated perovskite bottom surfaces. a-b, The PL (**a**) and TRPL (**b**) spectra of delaminated perovskite films (exposing buried surfaces) with and without GSCs. The photocarrier lifetime (578 ns) fitted from the TRPL spectrum of target film is longer than that for the pristine film (99 ns).

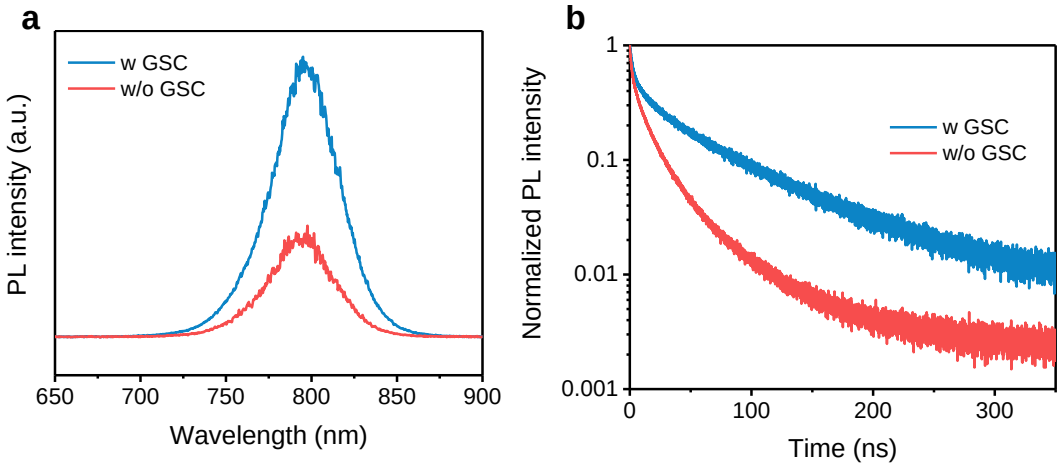

Supplementary Fig. 17. Bottom-side PL and TRPL measurement results of the quartz/SnO_2/perovskite structure. The PL (**a**) and TRPL (**b**) spectra of the samples with and without GSCs (with a structure of quartz/SnO_2/perovskite), measured from the quartz side. τ_{avg} decreases from 55 ns (pristine film) to 18 ns (target film).

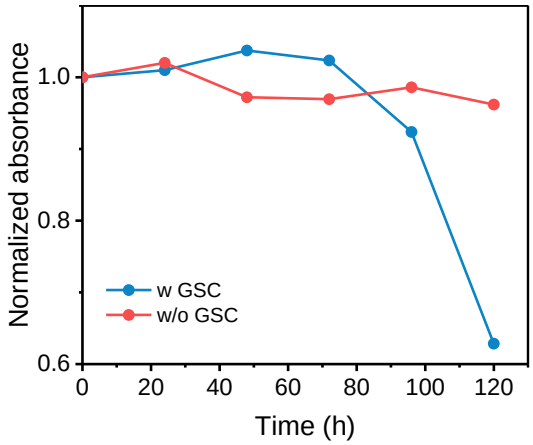

Supplementary Fig. 18. Absorption variations of perovskite films upon accelerated aging tests. The normalized absorbance variations at the wavelength of 700 nm for perovskite films with and without GSCs under accelerated aging tests (3-sun-intensity illumination; 80°C).

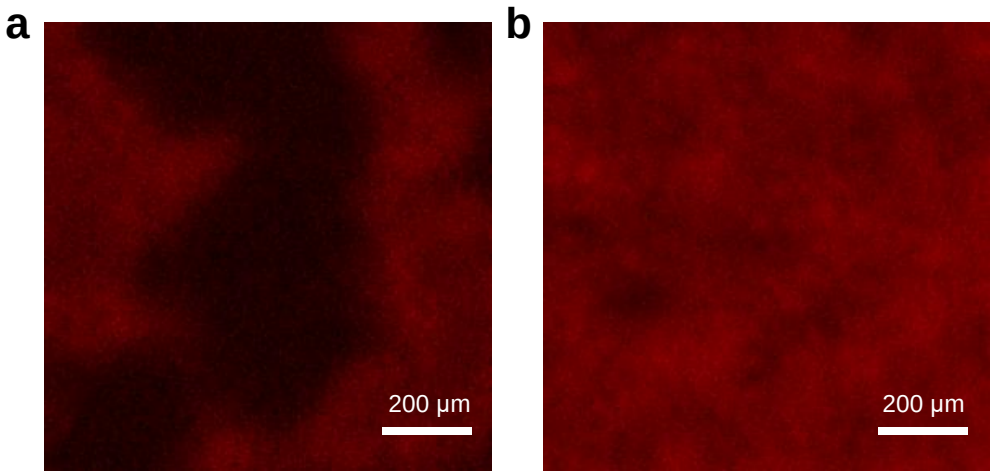

Supplementary Fig. 19. PL emission homogeneities of perovskite films after accelerated aging tests. The PL mapping images of perovskite grains with GSCs (**a**) and without GSCs (**b**) upon accelerated aging tests (3-sun-intensity illumination; 80℃) for 120 h.

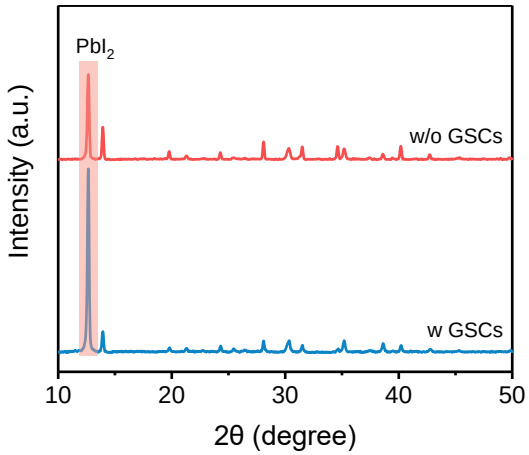

Supplementary Fig. 20. Phase evolutions of perovskite films after accelerated aging tests. XRD pattern of perovskite films with GSCs (**a**) and without GSCs (**b**) upon accelerated aging tests (3-sun-intensity illumination; 80℃) for 120 h.

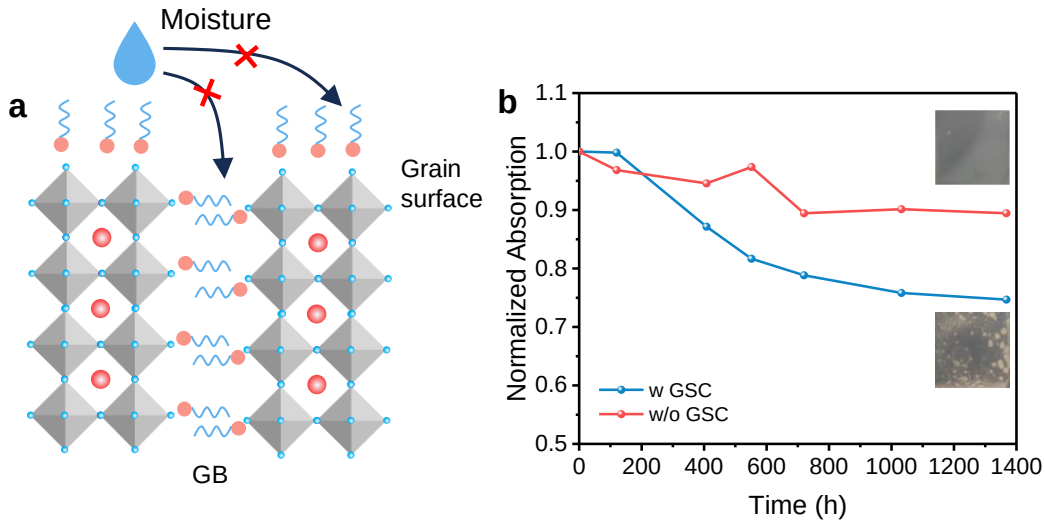

Supplementary Fig. 21. Moisture stability of perovskite films. a, Schematic illustration of TFSAP chemical functionalization on moisture tolerance. **b**, The normalized absorption of perovskite films with and without GSCs on 760 nm wavelength placed in an environmental condition with the humidity of 65-85 RH%. The inset is the optical photograph of perovskite after testing.

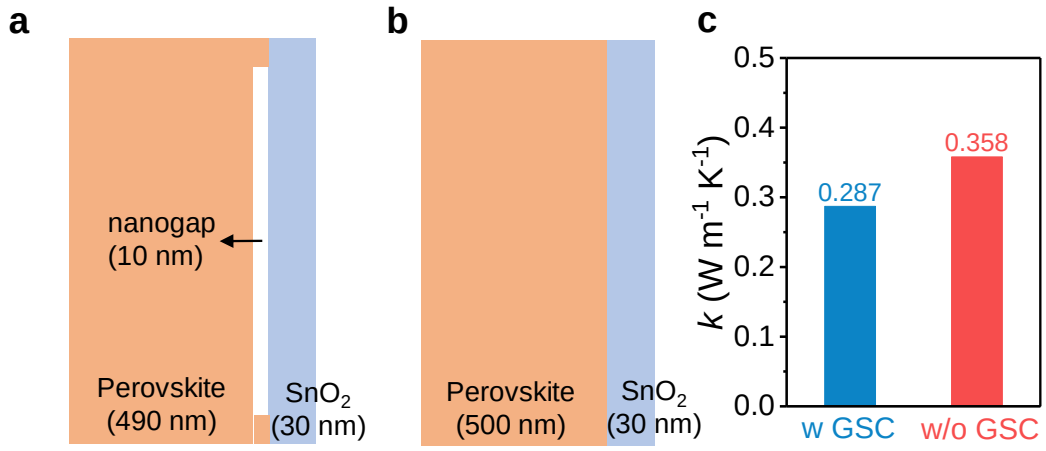

Supplementary Fig. 22. Simulated thermal conductivities of micro-heterointerfaces. The multilayer model for comparing the thermal conductivity with (**a**) and without GSCs (**b**), respectively. The height of perovskite and SnO_2 layer is 500 nm, with thickness labeled in the images. The shape of nanogaps induced by GSCs is simplified as a rectangle with a size of 460×10 nm^2.

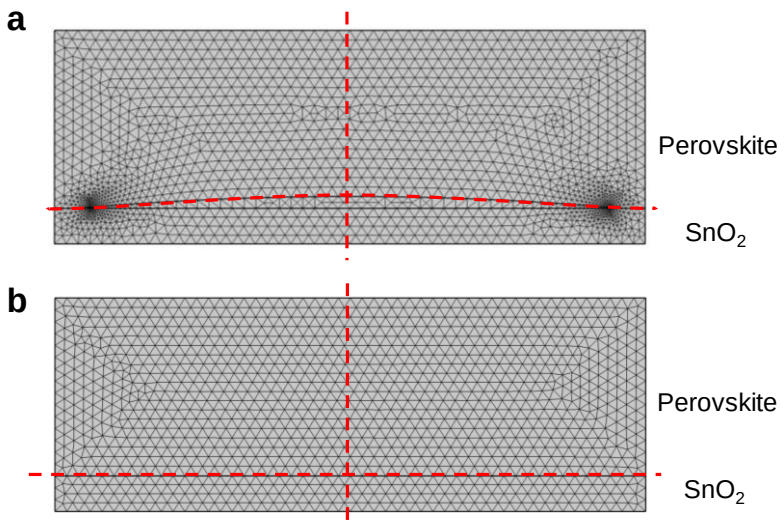

Supplementary Fig. 23. The model diagrams in FEA calculations. In the FEA calculation, the cross-sectional model diagrams of the grain-CTL micro-interface were generated for both cases with (**a**) and without GSCs (**b**). The nanogap induced by GSC is set as crescent-shaped structure at the heterointerface with a length of 460 nm and a depth of 10 nm. A longitudinal and a lateral guideline were labeled in both diagrams.

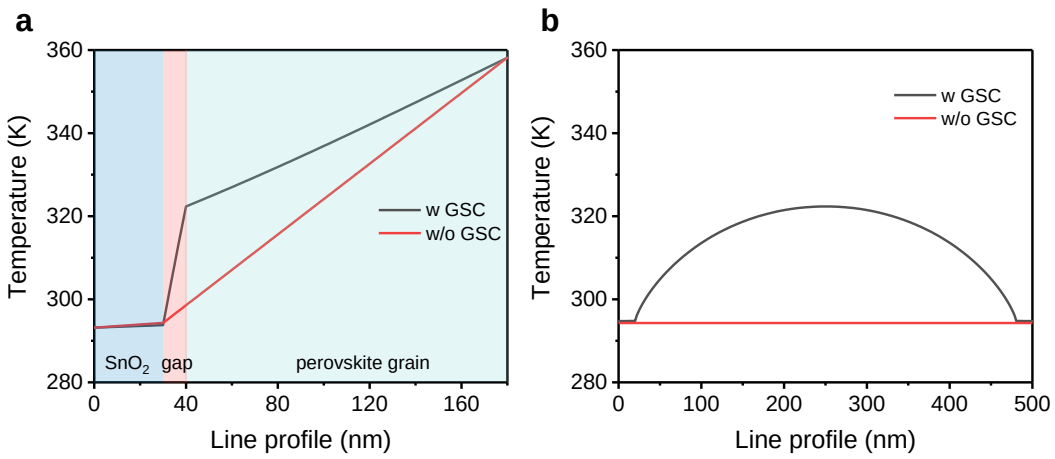

Supplementary Fig. 24. Evidence for GSCs causing interfacial thermal accumulation. The temperature line profile plot guided by longitudinal (**a**) and lateral line profile (**b**) at the bottom surface of perovskite grain with and without GSCs in **Supplementary Fig. 23**.

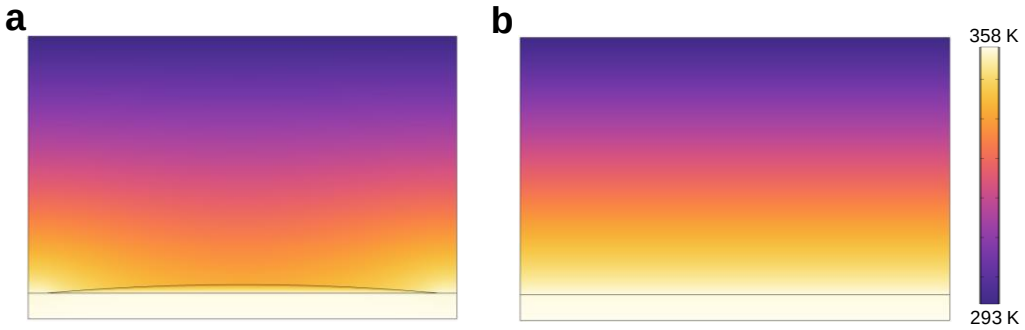

Supplementary Fig. 25. Temperature distributions at the micro-heterointerfaces. The temperature distributions of the grain-CTL micro-interface with (**a**) and without GSCs (**b**). The thermal source is set at the bottom surface of the SnO_2 layer. The temperature gradient is set from the bottom surface of the SnO_2 layer (85℃) to the top surface of the grain (20℃).

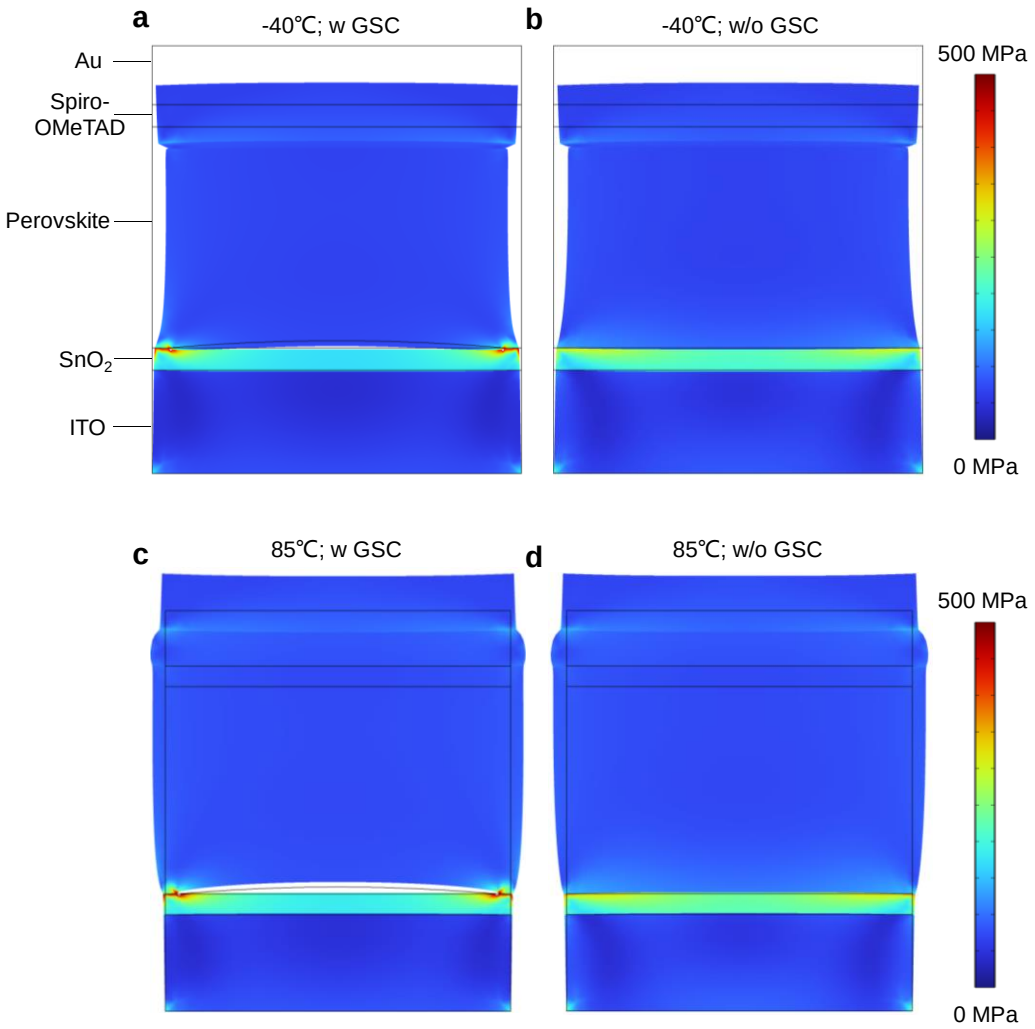

Supplementary Fig. 26. Simulated deformation and thermal stress of micro-heterointerfaces. The 2D elastic deformation and thermal stress distribution of perovskite films with (**a, c**) and without GSCs (**b, d**) of thermomechanical FEA results at -40℃ (**a, b**) and at 85℃ (**c, d**), respectively. The wireframe represents the device structure without deformation. The bottom surface of ITO layer is set as the rigid boundary considering the restriction of adjacent thick glass substrate to deformation. The micro-heterointerface shows the thermal stress accumulation at the junction point in the presence of GSCs.

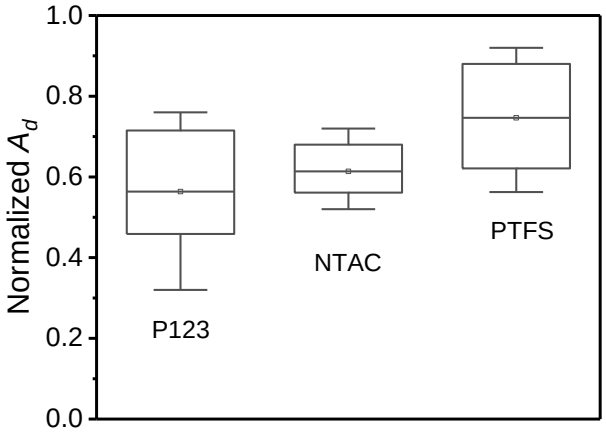

Supplementary Fig. 27. The influence of the GSCs existence on interfacial adhesion strength. Statistical distributions of the normalized delaminated area A_d after the delamination process of samples with P123, NTAC and PTFS based on 24 measurements in total. The box plot displays the mean, median line, upper minima and lower maxima, 25~75% box limits with 1.5× interquartile range whiskers.

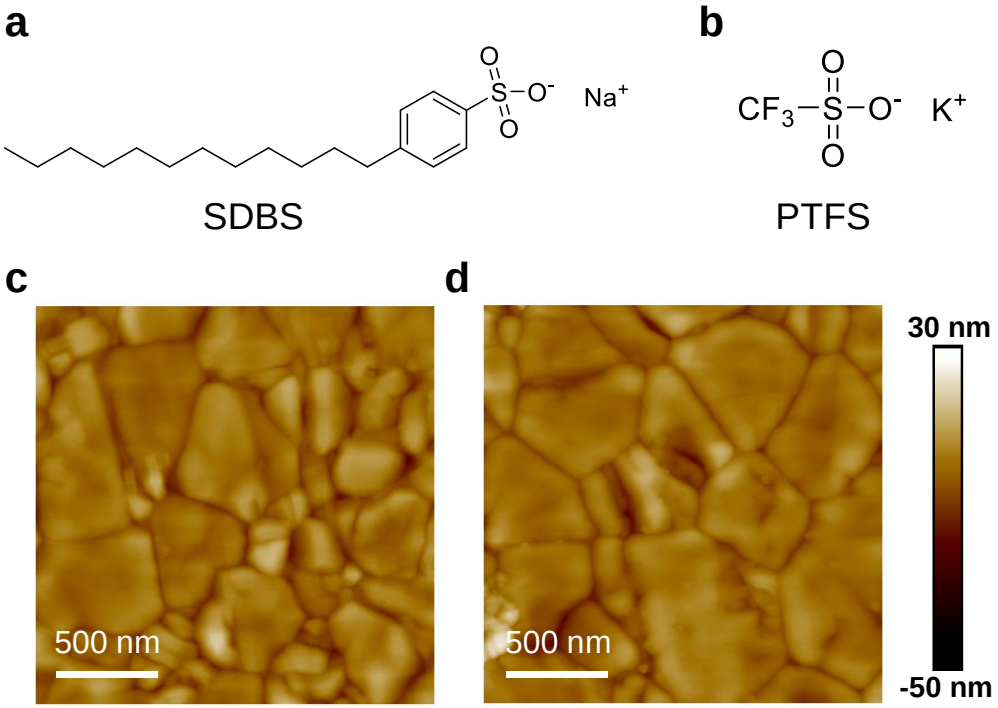

Supplementary Fig. 28. Limited morphologic effects on GSCs by two other selected molecules. a-b, The molecular structures of SDBS (**a**) and PTFS (**b**). **c-d**, The AFM topography image of the bottom surfaces of perovskite films at the perovskite-CTL heterointerface with additives of SDBS (**c**) and PTFS (**d**) into precursor solution.

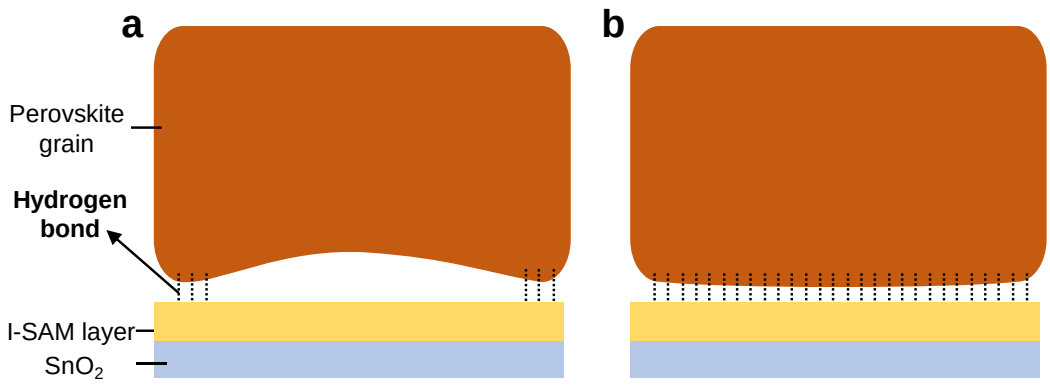

Supplementary Fig. 29. Proposed mechanism for minimum GSCs amplifying the benefits on interfacial adhesion using the I-SAM layer. Schematic illustration of the interfacial adhesion of perovskite grains with (**a**) and without GSCs (**b**). The I-SAM with –I terminated group can form a hydrogen bond with perovskite. The concaved central surface of grains with GSCs cannot form the hydrogen bond because of the existence of nanogaps at the micro-heterointerface.

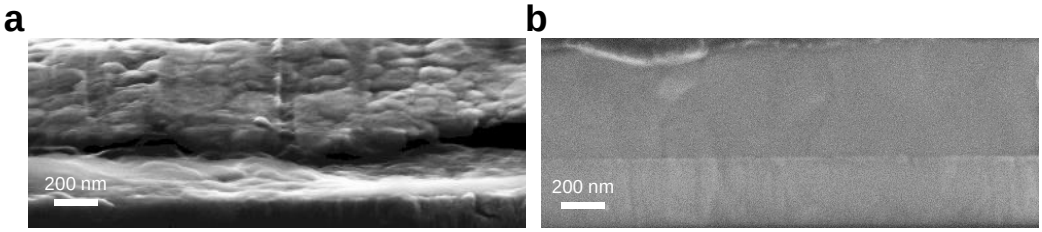

Supplementary Fig. 30 Perovskite film cross-sections after thermal cycling tests. The cross-sectional SEM images of perovskite films with (**a**) and without GSCs (**b**) after 300 cycles of thermal cycling tests (-40 to +85℃).

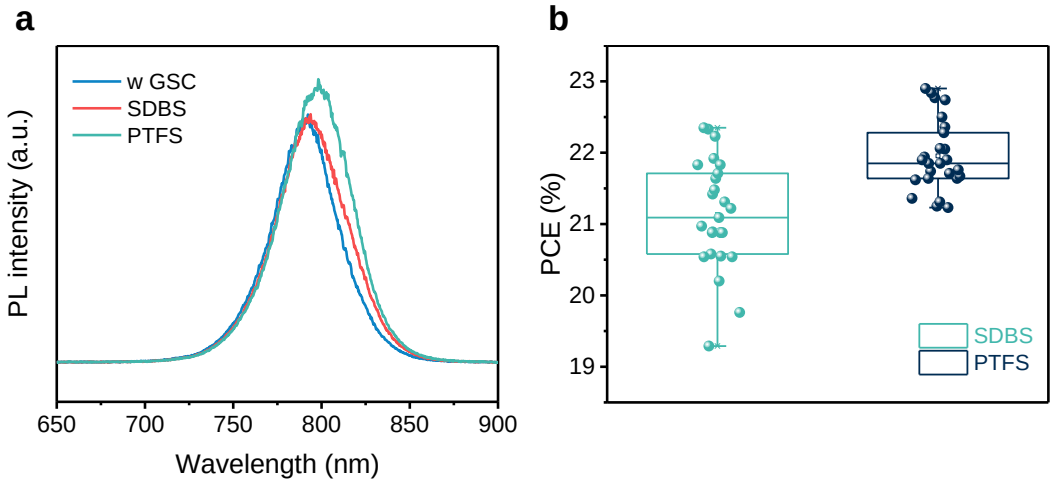

Supplementary Fig. 31. The limited levels of film property and device performance improvements attributed to chemical passivation only. a, The PL spectra of delaminated perovskite films (exposing buried surfaces) with GSCs, with SDBS, and with PTFS. **b**, PCE statistics of PSCs made with SDBS (sample size n = 25) and PTFS (sample size n = 25). The box plot displays the mean, median line, upper minima and lower maxima, 25~75% box limits with 1.5× interquartile range whiskers.

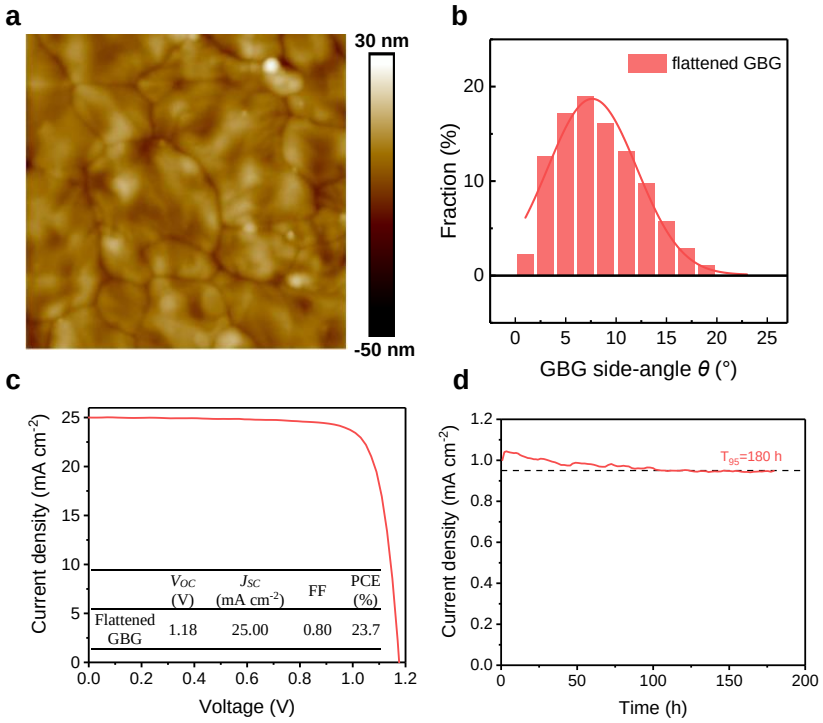

Supplementary Fig. 32. The limited level of device improvement attributed to GBGs flattening only. The AFM images of perovskite bottom surface (**a**) and statistical distribution of GBG side-angle θ (sample size, n=174) (**b**), J-V curve (**c**) and operational stability at MPP (**d**) of perovskite films/devices with flattened GBG. The inset table in (**c**) shows the extracted J-V parameters.

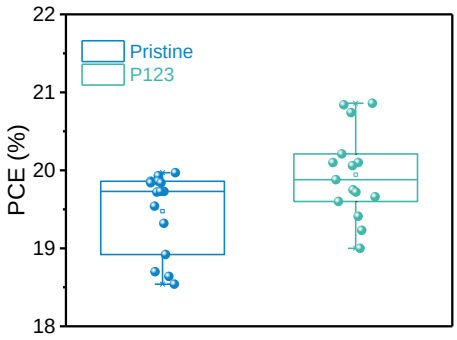

Supplementary Fig. 33 The influence of P123 on device PCEs. The PCE statistics of PSCs made without (pristine, sample size *n* = 15) and with Pluronic® P123 (sample size *n* = 15). The box plot displays the mean, median line, upper minima and lower maxima, 25~75% box limits with 1.5× interquartile range whiskers.

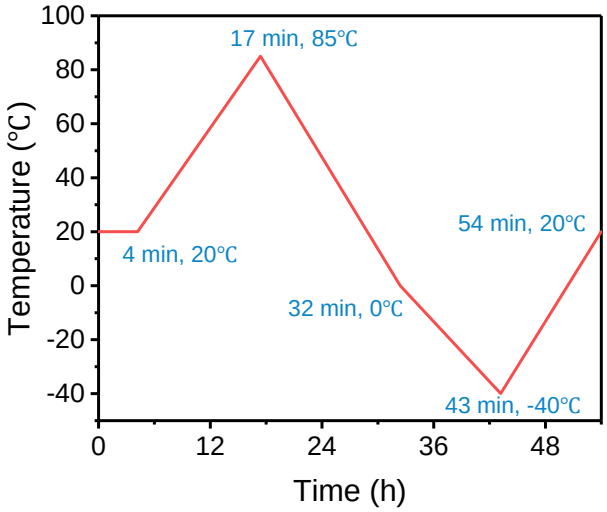

Supplementary Fig. 34. The temperature and time details for thermal cycling. The temperature variation curve of a cycle (54 min) during the thermal cycling test.

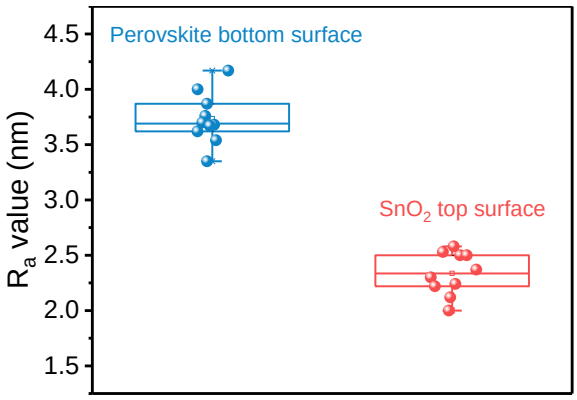

Supplementary Fig. 35. Negligible spatial differences in the topographies of perovskite bottom and SnO_2 top surfaces. Statistical distributions of R_a values for each AFM image (corresponding locations) of perovskite bottom surface (sample size n = 10) and SnO_2 surface (sample size n = 10). The box plot displays the mean, median line, upper minima and lower maxima, 25~75% box limits with 1.5× interquartile range whiskers.

Supplementary Table 1 The contact angles of water (H_2O) and diiodomethane (CH_2I_2) on perovskite films with and without GSCs.

Probing liquid	w GSC	w/o GSC
H_2O	58.3°	83.8°
CH_2I_2	33.7°	59.7°

Supplementary Table 2 The dispersive (γ_{lv}^{P}) and polar parts (γ_{lv}^{D}) of the surface tension of two probing liquids H_2O and CH_2I_2.

Probing liquid	γ_{lv} (mN m^{-1})	γ_{lv}^{P} (mN m^{-1})	γ_{lv}^{D} (mN m^{-1})
H_2O	72.8	43.7	29.1
CH_2I_2	50.0	2.6	47.4

Supplementary Table 3 The thermal conductivity k, heat capacity at constant pressure C_P, density ρ, Young's module M, Poisson's ratio v, and thermal expansion coefficient α in thermomechanical FEA.

	k (W m^{-1} K^{-1})	C_P (J kg^{-1} K^{-1})	ρ (kg m^{-3})	M (GPa)	v	α (K^{-1})
ITO	10.2	341	7120	116	0.35	5.81e-6
SnO_2	3.8	341	6950	401	0.28	6.80e-6
Perovskite	0.34	308	1368	20	0.33	5.80e-5
Spiro-OMeTAD	0.14	0.9	1020	2.5	0.35	3.59e-4
Au	315	126	19320	79	0.42	1.43e-5
Nanogap	0.023	1.004	1.225	/	/	/